Monitoring Persistent Coal Fire Using Landsat Time Series Data From 1986 to 2020

Xue Chen, *Graduate Student Member, IEEE*, Junhuan Peng, Zeyang Song, Yueze Zheng, and Biyao Zhang

***Abstract*— Coal fires pose great threats to valuable energy resources, the ecological environment, and human safety. They are one of the most persistent fires on the Earth, which can burn for an extremely long-term period from decades to hundreds or even thousands of years. Remote sensing detection of coal fires is of significance for mitigating coal fire hazards. Nevertheless, short-term or temporal discrete land surface temperature (LST) data have limited capability in characterizing the persistent coal fire. This study proposed a methodology to monitor persistent coal fires using long-term Landsat thermal images and further to analyze spatiotemporal dynamics of coal fires. A total of 1118 high-quality Landsat images (each image containing 446 × 446 pixels) spanning 35 years from 1986 to 2020 in the Wuda coalfield area (China) were processed to retrieve the LST. LST time series of each pixel was decomposed into the seasonal, trend, and remainder components. Coal fire areas were demarcated by using the range of the trend components. To trace the trend and change point of the LST time series, the Mann–Kendall test was applied to the trend components, and the Pettitt test was employed to the original time series vectors of those pixels located in the coal fire areas, respectively. The random sample consensus algorithm was utilized to identify the background temperature (inliers) and high temperature (outliers) and, thus, judge the coal fire burning period, and the symbolic aggregate approximation algorithm was used to evaluate the robustness of the judgment. The calibration was conducted according to the filed surveys, obtaining spatiotemporal 3-D coal fire dynamics. The proposed methodology was testified by comparisons with fieldwork and regional anomaly extractor algorithm, demonstrating good performance in comprehensive monitoring of persistent coal fires.**

Manuscript received October 19, 2021; revised December 10, 2021; accepted December 25, 2021. Date of publication January 12, 2022; date of current version March 14, 2022. This work was supported in part by the General Program of National Natural Science Foundation of China under Grant 42074004 and Grant 51804168, in part by the Ministry of Natural Resources of the People's Republic of China under Grant 0733-20180876/1, and in part by the China Postdoctoral Science Foundation under Grant 2018T110492 and Grant 2017M620209. *(Corresponding authors: Junhuan Peng; Zeyang Song.)*

Xue Chen is with the School of Land Science and Technology, China University of Geosciences, Beijing 100083, China, and also with the Department of Geosciences, University of Padua, 35131 Padua, Italy (e-mail: chenxue@cugb.edu.cn).

Junhuan Peng is with the School of Land Science and Technology, China University of Geosciences, Beijing 100083, China, and also with the Shanxi Key Laboratory of Resources, Environment and Disaster Monitoring, Jinzhong 030600, China (e-mail: pengjunhuan@163.com).

Zeyang Song is with the College of Safety Science and Engineering, Xi'an University of Science and Technology, Xi'an 710054, China (e-mail: songzeyang03@126.com).

Yueze Zheng is with the School of Land Science and Technology, China University of Geosciences, Beijing 100083, China, and also with the Photogrammetry and Remote Sensing Department, Beijing Institute of Surveying and Mapping, Beijing 100038, China.

Biyao Zhang is with the State Key Laboratory of Remote Sensing Science, Aerospace Information Research Institute, Chinese Academy of Sciences, Beijing 100094, China.

Digital Object Identifier 10.1109/TGRS.2022.3142350

***Index Terms*— Coal fires, land surface temperature (LST), Mann–Kendall test, Pettitt test, random sample consensus (RANSAC), symbolic aggregate approximation (SAX), time series decomposition.**

I. Introduction

COAL fires are a global environmental catastrophe [1], widely spreading in China [2]–[4], India [5], [6], the USA, South Africa, Indonesia, Russia, and Australia. They refer to the uncontrollable combustion of coal, which often occurs underneath the ground surface and is triggered by mining operations. Subsurface fires can occur in unmined coal beds when an outcrop ignites, and the combustion front subsequently propagates along with the buried coal seam into deeper geological rocks. Coal combustion and gasification collapse results in ash and void areas, and forms the fissures, which contributes to the exchanges of gases between the surface and the coal seam, and accelerates the burning [7]. The fires can continue to burn for an extremely long-term period of hundreds or thousands of years [8] until the fuel is completely burned out [5]. Monitoring the coal fire dynamics is of utmost necessity for understanding, prevention, and mitigation of coal fire hazards [5]. Multiple detection techniques such as geophysical [9]/geochemical [10], [11], detection and spaceborne [12]/airborne [8], [13], and remote sensing detection have been used to demarcate and monitor coal fires. Among these approaches, spaceborne remote sensing technology is most commonly employed because it provides cost-effective large-scale high-resolution thermal infrared (TIR) data and avoids direct contact with dangerous high-temperature and subsidence areas [13]–[18].

Currently, algorithms using TIR remote sensing for demarcating coal fire and monitoring coal fire dynamics can be roughly grouped into two categories: 1) monotemporal methods, including density slicing thermal imagery with fixed or varying thresholds [19]–[21], the moving window-based method [12], [22], and the self-adaptive gradient-based thresholding method [23] and 2) multitemporal methods, including automatically delineation from multispectral satellite data [22], stacking the coal fires [24], [25], image-differencing algorithm [23], and so on. It is hard for the methods mentioned above to mitigate the error and misinterpretation of individual LST pixels caused by the environmental context due to the lack of temporally correlated information. Moreover, coal fire persistently burns for an extremely long period. The short-term multitemporal methods divide persistent coal fires into several discontinuous "slices" and observe them from the short-term perspective. They fail to improve the under-

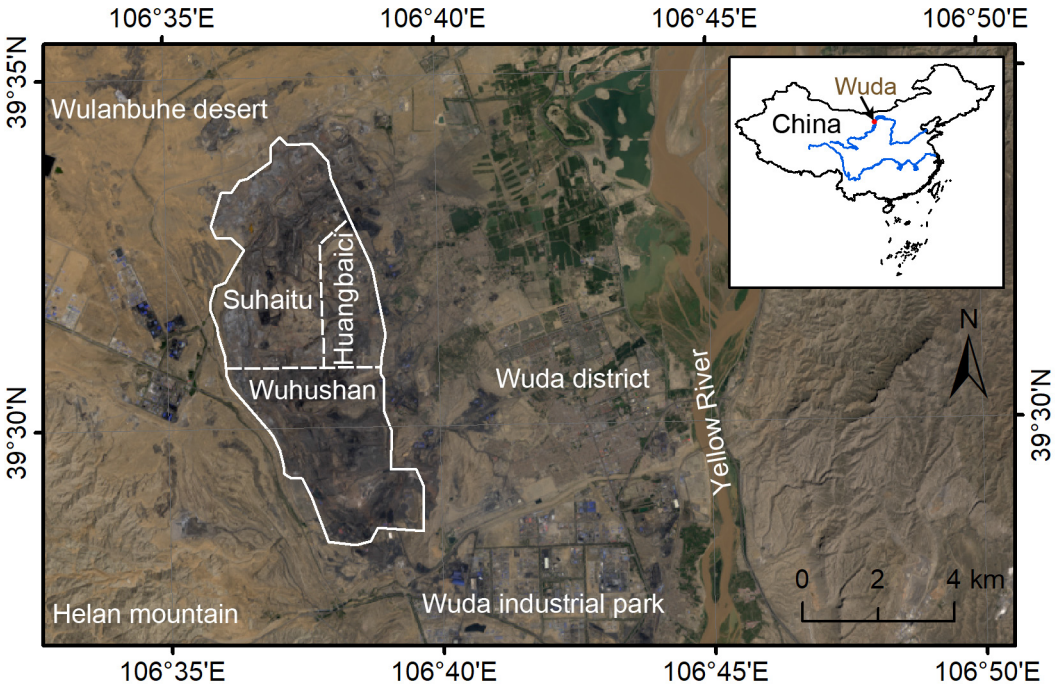

Fig. 1. Location of the study area, modified from [39]. Basemap credit: Landsat 8 OLI/TIRS images from United States Geological Survey date August 13, 2020.

standing of the spatiotemporal evolution from the life-cycle point of view [26]. By contrast, long-term monitoring takes advantage of holistically characterizing the burning stages and predicting the coal fire propagation. Pandey *et al.* [27] produced a temporal transition map during the years 1988–2013 based on the spatial distribution of thermal anomalous area in Jharia coalfield using overlay analysis of six images in every successive five years. Jiang *et al.* [28] assessed the status and effectiveness of the underground coal fire suppression efforts in Wuda coalfield using eight Landsat images from 2000 to 2015. Mishra *et al.* [29] extracted the coal fire map from four Landsat images at a five-year interval in 2001–2016, showing the propagation direction and the status of coal fires. Although, in these studies, the time span of satellite images was larger than ten years, imagery data are quite sparse due to less than one thermal infrared image per year. Mujawdiya *et al.* [30] first proposed the application of time series decomposition in pixel scale for detecting and characterizing coal fire using 782 available MODIS LST products spanning 2001–2017 in several typical coal fire pixels with about 1-km spatial resolution, in which the Mann–Kendall method [31], [32] was used for the background annual trend segmentation. However, the low spatial resolution of MODIS images was not beneficial for coal fire demarcation.

In this study, we propose an approach for medium-resolution (30 m) long-term (35 years) pixelwise LST time series analysis to demarcate coal fire areas and characterize the persistent dynamics. The statistical information of trend components is used as a criterion to identify the coal fire areas. The Mann–Kendall test [31], [32] and the Pettitt test [33] are applied for the trend and change point detection in these coal fire areas. The random sample consensus (RANSAC) algorithm [34] is utilized to the coal fire pixels identifying background temperature when there were no fires and further to judge the coal fire burning period, and the symbolic aggregate approximation (SAX) algorithm is used to evaluate the robustness of the judgment. The advantages of this methodology include addressing the uncertainty caused by data quality [35] and preprocessing, capturing the persistent features of coal fire dynamics, and providing a comprehensive understanding of the spatiotemporal patterns of coal fire hazards.

This article is organized as follows. Section II presents the study area and the data sources. Section III provides the methodology and associated theoretical framework. The results of the case study are performed in Section IV and are comprehensively discussed in Section V. The conclusions are drawn in Section VI.

II. Study Area and Data Sources

A. Study Area

The study area is located in the Wuda district of Wuhai City, Inner Mongolia Autonomous Region, China (see Fig. 1). The area has a strongly continental climate. The annual precipitation is 168 mm, and evaporation is 3500 mm [36]. The average annual temperatures are around 9 °C with a minimum of −26 °C and a maximum of 40 °C [37], respectively. The land cover mainly includes coal and coal waste, sediments, metamorphic and pyrometamorphic rocks, vegetation, and water [38].

The coal-bearing strata originate from the Pennsylvanian and Permian ages [40]. The first recorded coal fire in the Wuda coalfield was in 1961 when self-ignition occurred in the Suhaitu Coal Mine and was then frequently detected in the following decades. In 1978, there were only six coal fire areas,

while the number increased to 16 and 18 in 2000 and 2004, respectively, and even more in 2010 [41]. Fire-fighting activities were started in early 2000 and undertaken on a large scale since 2006. The activities are scheduled to be finished by the year 2013 when all coal fires should have been extinguished. However, field surveys showed that blasting and excavation operations contribute to spontaneous combustion [39], [42], and even abandoned coal waste piles began to ignite [39].

B. Data Sources

1) Landsat Data: Short-wave and thermal infrared Landsat series data have been acquired and archived since 1982. Landsat 5 Thematic Mapper (TM), Landsat 7 Enhanced Thematic Mapper Plus (ETM+), and Landsat 8 Operational Land Imager (OLI) and Thermal Infrared Sensor (TIRS) are three of the Landsat series of the National Aeronautics and Space Administration. The series data are available on the Earth Explorer websites and have been widely utilized to retrieve LST. The failure of the scanline corrector (SLC-off) caused gaps in the Landsat 7 ETM+ data, resulting in approximately 22% data loss in each image. These gaps are treated as void values. Landsat 8 TIRS measures land surface temperature in two thermal bands (bands 10 and 11). Artifacts can be observed in the TIRS data, including banding and absolute calibration discrepancies. Some calibration has been done to keep the consistency in the whole Landsat archive [35], [43], [44]. A total of 1118 high-quality cloud-free thermal infrared images acquired between July 31, 1986, and November 1, 2020, in the Wuda coalfield area, were used. Two paths of images, which are path 130 (row 32) and path 129 (row 33), covered the study area. The acquisition time of Landsat images is shown in Fig. 2. The coordinate ranges are 106.58–106.7 °E longitude and 39.46–39.58 °N latitude, and thus, the numbers of pixels in the east–west and south–north directions are 446 and 446.

2) Field Survey Data: Field survey data associated with thermal anomalies in 2002, 2003, 2004, 2005, 2006, 2008, 2010, 2014, and 2018 were collected from the literature [12], [36], [39], [41], [42]. The field data were collected mainly by using a handheld radiant thermometer and a global positioning system (GPS) device for navigation. In the fieldwork on September 23, 2002, the surface temperatures were measured using thermometers and GPS receivers [12]. Field data in 2003, 2006, and 2008 were collected through airborne thermal surveys and fieldwork campaigns [36]. In 2004, 2005, and 2010, a very detailed survey was taken in an approximately regular grid with a radiometer and a GPS device [41]. Stable thermal anomalies from June 2013 to July 2014 were delineated according to thermal anomalies identified from Landsat-8 data using the regional anomaly extractor (RAE) algorithm and confirmed in May 2014 by fieldwork using a thermometer and a GPS device [42]. In January 2018, a field survey was taken for investigating smoke spots and coal fire spots [39].

III. Methodology

The overall workflow is shown in Fig. 3. In the first part, the multitemporal LST data are retrieved from Landsat images by using an open-source code [45] in the Google Earth Engine (GEE) platform. The high-quality LST data generate pixelwise time series vectors at all pixels at a temporal scale of 16 days or multiples of 16 days for each path.

The second part details the application of the LST time series decomposition method. The seasonal trend decomposition based on locally weighted regression smoother (STL) method [46] is applied, where seasonal smoothing and trend smoothing processes are repeated several times to improve the accuracy of the estimations of the seasonal, trend, and remainder components.

The mean, standard derivation, and the range (the difference between the highest and lowest) values of the trend component of each pixel are calculated, and the range values are used to identify the coal fire areas. The Mann–Kendall test [31], [32] and the Pettitt test [33] are applied on the pixelwise trend components vectors and the original pixelwise LST time series vectors at those pixels located in the coal fire areas, respectively, detecting the trend and the change point of the long-term coal fire dynamics. The random sample consensus (RANSAC) algorithm [34], estimating the parameters optimally fitting the data with outliers, is applied on the trend components. It was used to detect the background temperature and further to judge the coal fire burning period. LST values greater than the fit line (background temperature) by a given value are considered to be within the coal fire burning period. To evaluate the robustness of the judgment, the symbolic aggregate approximation (SAX) algorithm is applied to check the position of the fit line in the range of the LST values. Finally, the calibration and validation of long-term coal fire dynamics are conducted through the coal fire zones obtained from field surveys and the RAE [22], [42] algorithm.

A. Land Surface Temperature Retrieval

LST is estimated from the Landsat series images using the GEE open-source code [45]. GEE, launched in 2010 and powered by Google's cloud infrastructure, is a cloud-based platform that enables big data analyses without computation resources [47]. The platform provides a data catalog that stores a large quantity of geospatial data, including climate and weather data, spaceborne and airborne optical and radar imagery, and geophysical datasets [47]. All the Landsat Level-1 and Level-2 data can be queried, visualized, and analyzed on GEE, including top-of-atmosphere (TOA) and surface reflectance data.

Ermida *et al.* [45] provided the open-source code repository for computing LST from Landsats 4, 5, 7, and 8, which can help to monitor long-term coal fires. The Landsat series data are intercalibrated, and all TIR bands have been resampled to 30-m spatial resolution. In their method, the input data include Landsat data, atmospheric data, and surface emissivity. The LST is retrieved by using the statistical mono-window algorithm developed by the Climate Monitoring Satellite Application Facility [48]. The method is based on an empirical relationship between TOA brightness temperatures and LST.

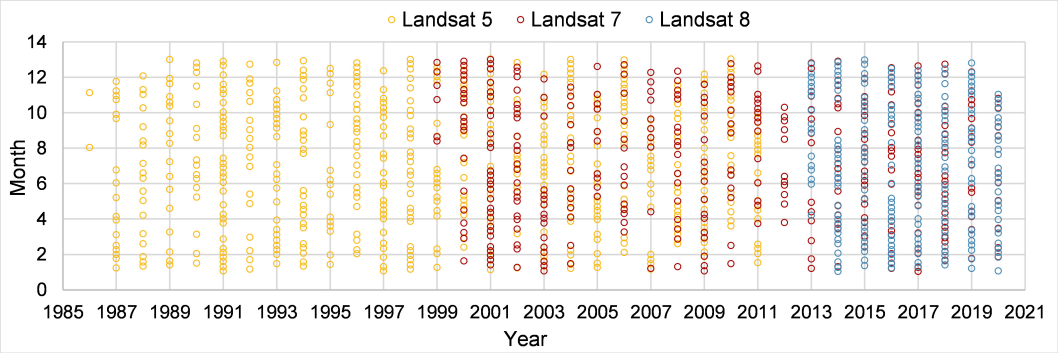

Fig. 2. Acquisition time of Landsat images used in this study.

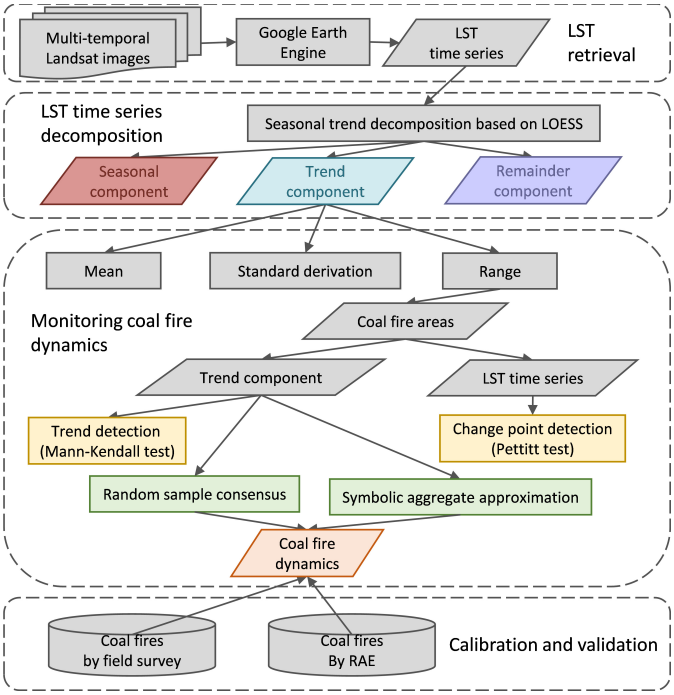

Fig. 3. Overall workflow of this study.

They build a simple linear regression model

$$\mathrm{LST} = A_i \frac{Tb}{\varepsilon} + B_i \frac{1}{\varepsilon} + C_i \tag{1}$$

where Tb is the TOA brightness temperature in the TIR channel and ε is the surface emissivity for the same channel. The algorithm coefficients A_i, B_i, and C_i are determined from linear regressions of radiative transfer simulation. They were obtained by the calibration database, which has been derived by using a dataset of air temperature, water vapor, and ozone profiles.

The quality of the algorithm is evaluated by comparing the retrieved LST data with observations from *in situ* LST stations, where the land cover includes grassland, shrubland, cropland, desert, and savanna. The overall root mean square errors from the 12 stations are 1.3 K, 1.1 K, and 1.0 K for Landsats 5, 7, and 8, respectively. Detailed information can be referenced in [45].

B. Seasonal Trend Decomposition Based on LOESS

The seasonal trend decomposition based on LOESS (STL) [46] method is applied in this study, which has also been used in Mujawdiya *et al.*'s study [30]. LOESS is short for locally weighted regression smoother. The STL procedure is implemented in an iterative cycle of detrending and updating the seasonal component. The iterative cycle includes two recursive procedures: an outer loop and an inner loop nested inside the outer loop. Each pass of the inner loop applies seasonal smoothing and trend smoothing that updates the seasonal and the trend components [46].

The most attractive feature of the STL decomposition is its strong resilience to outliers, generating versatile and robust components [49]. Furthermore, it can handle any type of seasonality data and is not restricted to monthly, quarterly, and annual data. Besides, the STL procedure is implemented relying on numerical methods, and thus, it does not need mathematical modeling. The disadvantages are that it does not handle calendar variation automatically, and it is only appropriate for additive decompositions. The STL decomposition procedure can readily be implemented in the R language using the function "stl" [50] and in the Python language [51] using the function "stldecompose" provided by Josh Montague.

In detail, in this study, using the Python language, the LST time series calculated from Landsat images are resampled to every eight days. For the period, an input parameter that represents the most significant periodicity in the time series observations is set to 46; the "lo_frac," which is the fraction of data to use in fitting Lowess (locally weighted scatterplot smoothing) regression, is set to 0.09, indicating that the smoothing window is about three years; and the "lo_delta," which is the fractional distance within which to use linear interpolation, is set to 0.01, as the default.

C. Monitoring Coal Fire Dynamics

1) Mann–Kendall Test for Trend Detection: For trend detection, the Mann–Kendall test is the most commonly used method. The Mann–Kendall test, proposed by Mann [31] and Kendall [32], is a nonparametric test to statistically assess whether a time series has a monotonic upward or downward trend. The null hypothesis H_0 is that the data are independently and randomly ordered without monotonic trend, and

the alternative hypothesis H_1 is that the data have a monotonic trend.

For the time series $x_1, \ldots, x_n$, the test statistic of the Mann–Kendall test is

$$S_{mk} = \sum_{i=1}^{n-1} \sum_{j=i+1}^{n} \operatorname{sgn}\{x_j - x_i\} \tag{2}$$

where

$$\operatorname{sgn}\{x_j - x_i\} = \begin{cases} 1, & x_j - x_i > 0 \\ 0, & x_j - x_i = 0 \\ -1, & x_j - x_i < 0. \end{cases} \tag{3}$$

S_{mk} is asymptotically normally distributed. Under the null hypothesis, when there are no ties in data, it has expectation and variance as follows:

$$\begin{aligned} E[S_{mk}] &= 0 \\ \operatorname{Var}[S_{mk}] &= n(n-1)(2n+5)/18. \end{aligned} \tag{4}$$

Providing that the following Z-transformation is employed:

$$Z_{mk} = \begin{cases} \dfrac{S_{mk} - 1}{\sqrt{\operatorname{Var}[S_{mk}]}}, & \text{if} \quad S_{mk} > 0 \\ 0, & \text{if} \quad S_{mk} = 0 \\ \dfrac{S_{mk} + 1}{\sqrt{\operatorname{Var}[S_{mk}]}}, & \text{if} \quad S_{mk} < 0. \end{cases} \tag{5}$$

If $Z_{mk} > 0$, it indicates an increasing trend. Given a certain confidence level α, if $|Z_{mk}| > Z(1 - \alpha/2)$, the sequential data would have a statistically significant trend. Here, $Z(1 - \alpha/2)$ is the corresponding value of $P = \alpha/2$ following the standard normal distribution. $\alpha = 0.05$ was adopted as the confidence level in this study. The approximate p-value is then calculated as

$$p_{mk} = 2\min(0.5, P(X > |Z_{mk}|)), \quad X \sim n(0, 1). \tag{6}$$

Besides, the magnitude of the trend is estimated by Sen's slope, which is

$$\beta = \operatorname{Median}\left(\frac{x_j - x_i}{j - i}\right), \quad j > i. \tag{7}$$

If $\beta > 0$, it indicates an upward trend and, otherwise, a downward trend. The Mann–Kendall test procedure can be implemented in the Python language using the function "pymannkendall" provided by Shourov *et al.* [52].

2) Pettitt Test for Abrupt Change Point Detection: For change point detection, the Pettitt test [33] is the most commonly used method because of its sensitivity to breaks. It assumes that the observations generate an ordered sequence of observations. Initially, the distribution of the sequences has one location parameter, and at some point, there is a shift in the location parameter. The null hypothesis H_0 is that the variables follow the same distribution; thus, there is no change in the location parameter, and the alternative hypothesis H_1 is that there is a change in the location parameter.

The Pettitt test is a rank-based nonparametric sign test, which is based on the Mann-Whitney two-sample test. The most probable change point t satisfies

$$S_t = \max\left|\sum_{i=1}^{t} \sum_{j=t+1}^{T} \operatorname{sgn}\{x_j - x_i\}\right|. \tag{8}$$

Under the null hypothesis, the distribution of S_t is symmetric around zero with $E(S_t = 0)$. When there is a shift in the sequence of observations, it is expected to have large values for S_t. For the continuous observations, they follow

$$\sum_{i=1}^{t} \sum_{j=t+1}^{T} \operatorname{sgn}\{x_j - x_i\} = 2\sum_{i=1}^{t} r_i - t(T+1) \tag{9}$$

where r_i is the corresponding rank of data point x_i. The significance probability p_t associated with value S_t can be approximately evaluated as

$$p_t = 2\exp\left\{\frac{-6S_t^2}{T^2 + T^3}\right\}. \tag{10}$$

Given a significance level α, if $p_t < \alpha$, the null hypothesis is rejected, and a conclusion that there is a change point at level α is drawn. The Pettitt test procedure can be implemented in the Python language using the function "pyhomogeneity" provided by Shourov *et al.* [52].

In detail, in this study, the Pettitt test is iteratively applied according to the characteristic of homogeneity. If the time series is nonhomogenous, the change point is accepted, and the change point detection is continuously applied on the subtime series. If the period is homogenous, the change point is rejected, and the detection moves to the next subtime series. To avoid too many change points within one year, in which case the mean LST values would be either too high or too low, the minimum period of subtime series was set to 1 year.

3) Random Sample Consensus (RANSAC) Algorithm: The random sample consensus (RANSAC) algorithm, proposed by Fischler and Bolles [34], is an algorithm for the robust fitting of models when many outliers are presented in the dataset [53]. The basic step is summarized as follows [53].

1) Randomly select the minimum number N points from totally M points.
2) Estimate parameters for the model.
3) Determine the numbers of points that fit the model within a predefined tolerance.
4) If the ratio of the number of inliers to the total number points exceeds a predefined tolerance, reestimate the parameters using all the identified inliers and terminate.
5) Otherwise, repeat steps 1)–4) for L times.

L can be defined as

$$L = \frac{\log(1 - p)}{\log\left(1 - u^N\right)} \tag{11}$$

where p is the probability of a randomly selected point being part of a good model. u represents the probability of the selected data point being an inlier.

An advantage of RANSAC is its ability to make a robust estimation, estimating the parameters with a high degree of accuracy in the presence of a significant number of outliers [54]. The RANSAC processing can be implemented by using the function "ransac" in MATLAB [55].

In detail, the sample size is set to 2, and the maximum allowable distance for inliers is set to 1. The RANSAC algorithm in this study is changed a little to restrict the fit line horizontal to adapt to the characteristics of the change of LST, assuming that the background temperature, when there was no fire, is constant.

4) Symbolic Aggregate Approximation (SAX) Algorithm: Symbolic aggregate approximation (SAX) is one of the extensions of the piecewise aggregate approximation (PAA), which represents time series in terms of symbols. PAA is a popular and simple way of reducing the dimensionality of the time series by splitting them into equal-sized segments and replacing the time series with averaged values in each segment. It transforms a time series $X = (x_1, \ldots, x_n)$ into another time series $\tilde{X} = (\tilde{x}_i, \ldots, \tilde{x}_m)$ with $m < n$. If m divides n, then

$$\tilde{x}_i = \frac{m}{n} \sum_{j=(n/m)\cdot(i-1)+1}^{(n/m)\cdot i} x_j. \tag{12}$$

SAX assigns a string representation to the time series. The time series data can be stored less than other data mining methods, e.g., discrete Fourier transform and wavelet transformation.

In this study, the most important role of the SAX method is to judge the position of the fit line from the RANSAC algorithm in the range of the LST trend component. As assumed before, in the RANSAC algorithm, the fit line is used as an indicator for calculating the background temperature. It is a standard line for the classification of the coal fire period. If the fit line is located at the bottom of the range of the LST trend component, the detected background LST value could be accurate and robust. If the fit line is at the top of the LST trend component, it is not believable. SAX in this study can also be used as a simple time series representation with reduced dimensionality.

In detail, the original LST time series is divided into 35 segment parts, being each subtime series spanning one year. The values of each time series are normalized, involving subtracting the mean of each observation and then dividing by the standard deviation. The range of the value is divided into four parts, from low values (bottom) to high values (top), with the symbol "low," "medium low," "medium high," and "high." Then, the location of the fit line from RANSAC is evaluated. If the line is located in "low" or "medium low," the result will be accurate and robust. If not, the result should be modified according to the field surveys.

IV. Results

A. LST Retrieval and Time Series Decomposition

The LST at each available Landsat acquisition was retrieved. The distribution of the LST values was highly consistent with the coal fire zones detected from the field surveys [12], [36], [39], [41], [42], the elevation, and the land use [41], [56]. High-temperature pixels were located not only in the coal fire zones but also in the Gobi-desert-sand, bareland, coal layer, coal dust, and mixed sandstone with shale areas. The low temperature indicated the agriculture, urban area, and the high elevation area [56].

In noncoal fire areas within the coalfield, the LST has the same characteristic as the LST in the noncoalfield area. Therefore, it can be assumed that noncoalfield LST is a good proxy for nonfire LST within the coalfield. A reference noncoal fire time series was determined by averaging the LST values of pixels located outside the coalfield in each image [30]. This time series was decomposed into three components by applying the STL decomposition method showing the long-term average gradual changes of the LST trend in the background area [see Fig. 4(a)]. The seasonal component shows the characteristics of annual changes, with a maximum value of about 20 °C and a minimum value of about −25 °C. The trend component is smoothing with a change. The remainder component seems to be noise. A sparse sampling with a window of 500 pixels in space domain was applied in the whole study area, including pixels outside and inside the coalfield, and the trend components of all the sampled pixels were plotted in Fig. 4(b), showing that almost all the trends have similar oscillations and slightly increasing trends, similar to the average trend component in Fig. 4(a). Three potential reasons are contributing to this increasing phenomenon: (1) the shifted values introduced during the LST retrieval, (2) LST increase in the background land possibly related to the climate effect, or (3) smoothing processing in the decomposition algorithm. Anyway, the common trend was mitigated by subtracting the reference noncoal fire trend [see Fig. 4(a), trend components] from the trend components of all pixels. After the subtraction, most of the time series are changeless [see Fig. 4(c)] during the long period, indicating that they were possible not located in coal fire areas, while the trend with evident changes could be interpreted that the pixel is located in coal fire areas.

B. Monitoring Coal Fires Dynamics

1) Identification of Coal Fire Areas: After removing the reference noncoal fire trend, the mean, the standard deviation, and the range values of the trend component in each pixel were calculated and illustrated as maps shown in Fig. 5. The mean values map [see Fig. 5(a)] did not show evident differences inside and outside the coalfield. Some areas inside the coalfield had very high mean values, indicating that these areas were likely to have experienced coal fires. An area outside the coalfield in the northeast also had high mean values, which was possibly due to desert sand, coal dust, and coal processing operations [42], [57]. Besides, in the southeast area, there were low values because of the high elevation of the Wuhushan Mountain. The standard deviation values map [see Fig. 5(b)] showed that large values were mainly located inside of the coalfield, and the largest values were located in the center of the coalfield, indicating that there were large changes in the trend components. Five coal waste pile fire and two coal processing operations locations [42] [see Fig. 5(b)] also had high standard deviation values. The range values map [see Fig. 5(c)] showed very similar spatial characteristics to the standard deviation values map [see Fig. 5(b)], where most of the high values were located inside the coalfield. Large standard derivation values were also possibly caused by the

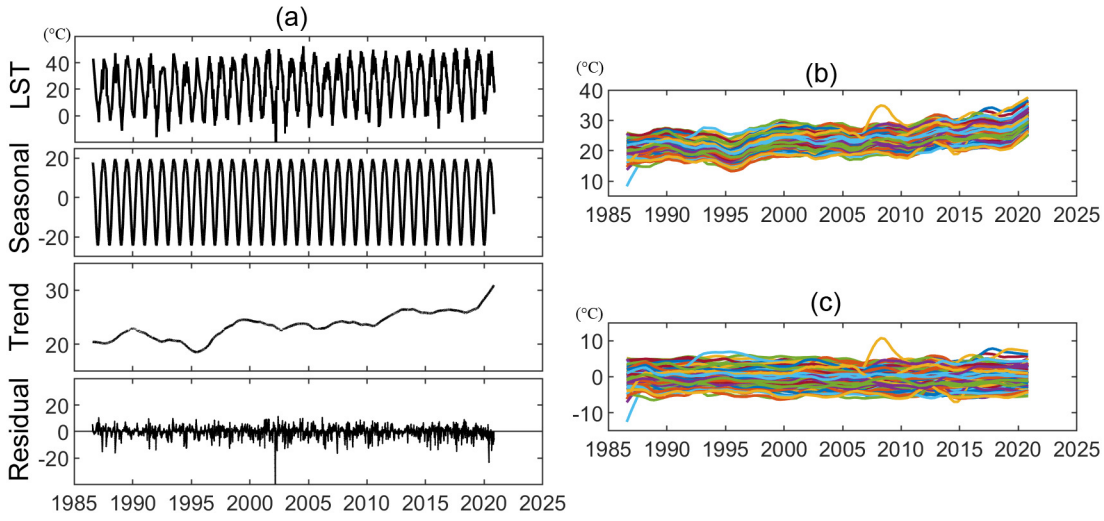

Fig. 4. STL decomposition of the reference noncoal fire time series (a), showing the average trend, seasonal, and remainder components. Trend components of sparsely sampled points in the whole study area (b) before and (c) after removing the reference noncoal fire trend.

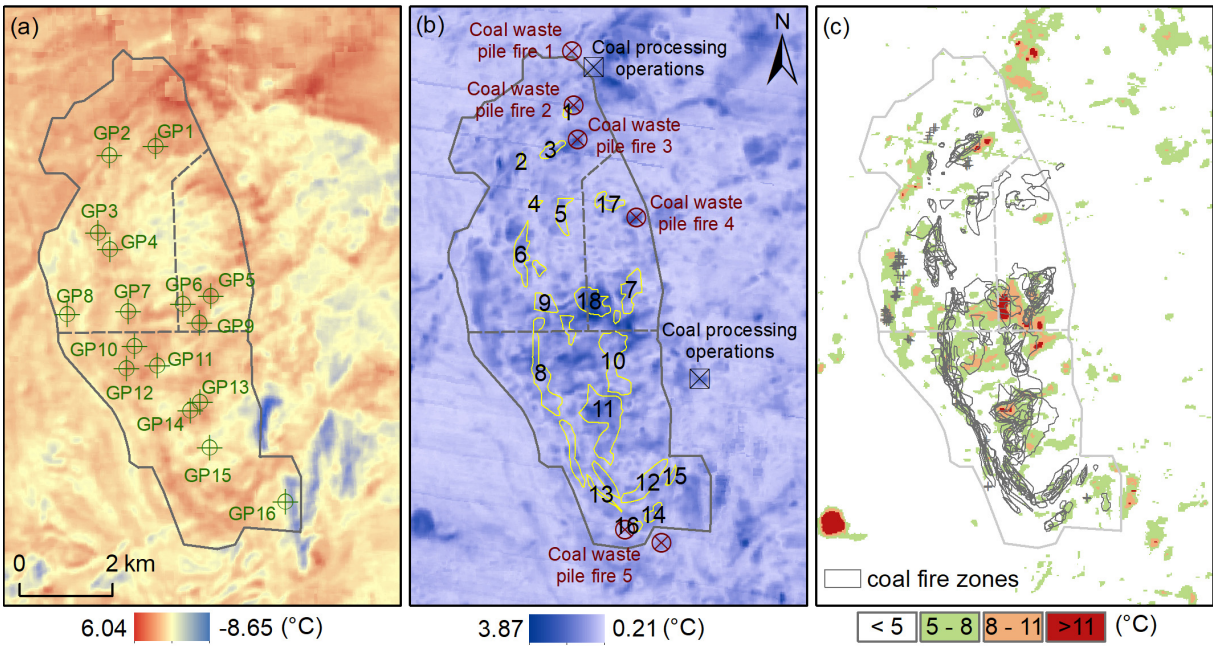

Fig. 5. (a) Mean, (b) standard deviation, and (c) range value maps of the trend component.

large LST oscillation related to the land cover types, while range values were more ascribed to the coal fire dynamics. Therefore, range values became the main factor to determine the coal fire areas. Considering the mean of the range values of trend components in the background area outside the coalfield, which is 2.97 °C, the range values higher than 3 °C were shown in Fig. 5(c), overlaid with coal fire zones from field surveys. The areas with range values higher than 5 °C were in good agreement with the coal fire zones; therefore, these pixels were recognized to be coal fire pixels. Taking into account Fig. 5(c) and the coal fire zones manufactured from the field surveys, 16 distributed ground points, named GP1–GP16, as shown in Fig. 5(a), were selected to test the proposed methodology.

2) Trend and Change Point Detection for Ground Points: The gradual changes of the LST time series at each ground point were detected by using the Mann–Kendall test on the trend component vector, showing the increasing or decreasing trend, and the slope values. The ground points GP8, GP10, and GP11 were detected without trends. The ground points GP2 (slope value −0.46 °C/year) and GP5 (slope value −1.43 °C/year) were detected having decreasing trends, and other ground points were detected with increasing trends. The slope values, where positive and negative values indicate increasing and decreasing trends, respectively, were not so large because of the long period of 35 years. Nevertheless, the trend and slope values can still indicate that the coal fire occurred during the early or late stage. The Mann–Kendall test

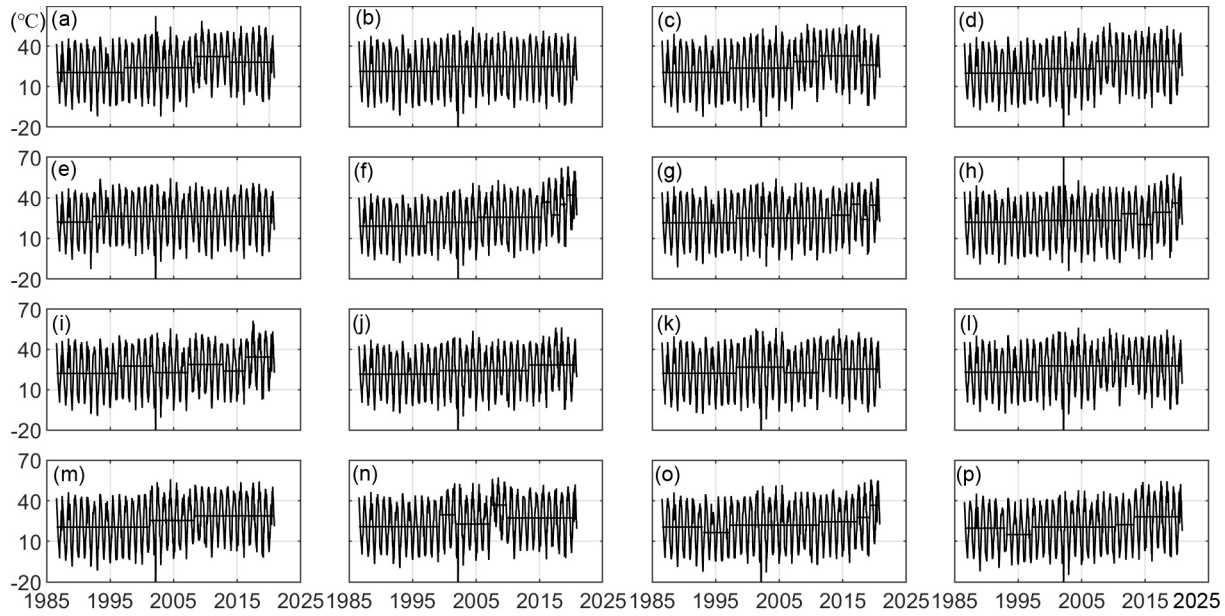

Fig. 6. LST time series of the ground points GP1–GP16, their respective change dates detected by the Pettitt test, and the mean LST values before and after the change dates. The horizontal straight lines in the subfigures are the mean values of the subtime series. (a) GP1. (b) GP2. (c) GP3. (d) GP4. (e) GP5. (f) GP6. (g) GP7. (h) GP8. (i) GP9. (j) GP10. (k) GP11. (l) GP12. (m) GP13. (n) GP14. (o) GP15. (p) GP16.

can be applied to a shorter period within about ten years, which will have a better performance. Some other time series analyses, such as knee point detection [58] and peak point detection [59], could be applied to describe the gradual changes.

The abrupt change points of the LST time series at each ground point were investigated by applying the Pettitt test on the original LST time series. The algorithm was iterated according to the characteristic of homogeneity. All the change points of the 16 ground points were shown in Fig. 6. Also, the mean LST values before and after the change points were plotted. The Pettitt test presented an accurate abrupt change date for the changes. In some short periods with large changes, the algorithm did not work so well, e.g., the last five or ten years in GP6, GP7, and GP8 [see Fig. 6(f), (g), and (h)]; the change points were too close.

Note that the trend and change point detection was not always essential and effective for all the pixels in this study. For one thing, most coal fires, especially underground ones, last for a long time, and their LSTs were not high enough to yield trend change or breakpoints. For another, methods could detect wrong or even opposite tendencies when detecting breakpoints in time series without breakpoints [60]. Therefore, trend and change point detection could be implemented only in those time series with large trend changes.

3) Temporal Evolution of Coal Fires at Ground Points: To judge the coal fire burning period, the RANSAC algorithm was applied to the trend component of the 16 ground points. The trend components and fit lines from the RANSAC algorithm were plotted in Fig. 7. Taking into account the mean range values of the pixels in the background, which is 2.97 °C, the threshold of background LST values range was set to ±1.5 °C. LST trend values that are at least 1.5 °C greater than the background LST trend values were shown in red color (see Fig. 7), which are more likely to be coal fire in that period. Those values that at least 1.5 °C lower than the background values were shown in blue color. RANSAC works better than least square to fit the background LST values in this case, where high changes of LST trend values would have a great effect on the regression estimation.

To evaluate the feasibility of the proposed method, the coal fire dynamics of the 16 ground points were validated with the coal fire zones from the field surveys and compared with coal fire zones detected from the RAE method. Ground points GP1–GP16 are mainly located in the coal fire zones (see Fig. 8). The coal fire or the hot spots were obtained in the years 2002–2010 by field surveys [12], [36], [39], [41], [42]; the new coal fire zones in 2014 were identified by the RAE method [22], [42]. The coal fire information extracted from the proposed methodology and the field survey/RAE method were listed in Table I before and after the "/." For ground points, GP1, GP6, GP8, and GP16, the coal fire burning period detected by our methodology was completely the same as the coal fire burning period from the field surveys and the RAE method. For GP2, GP3, GP11, GP13, GP14, and GP15, only one year of coal fire burning period was not consistent with the field surveys or the RAE results. GP9 and GP10 show two years' bias. GP4, GP5, GP7, and GP12 seemed to have evident biases with the field surveys. Nevertheless, if the fit lines of the four points were shifted down a bit, the situations from the proposed methodology and the field surveys or the RAE method will be much more similar. Especially, for GP12, the true background value seemed to be 2 °C lower than the fit line. In this case, after shifting the fit line down 2 °C, there were coal fires, which were close to the situation from the field surveys in the period 1995–2005, there were coal fires close to the situation from the field surveys. Fig. 8 shows four photos taken at GP7, GP9, GP10, and GP13 in 2014 *in situ* field campaign (modified from [42]).

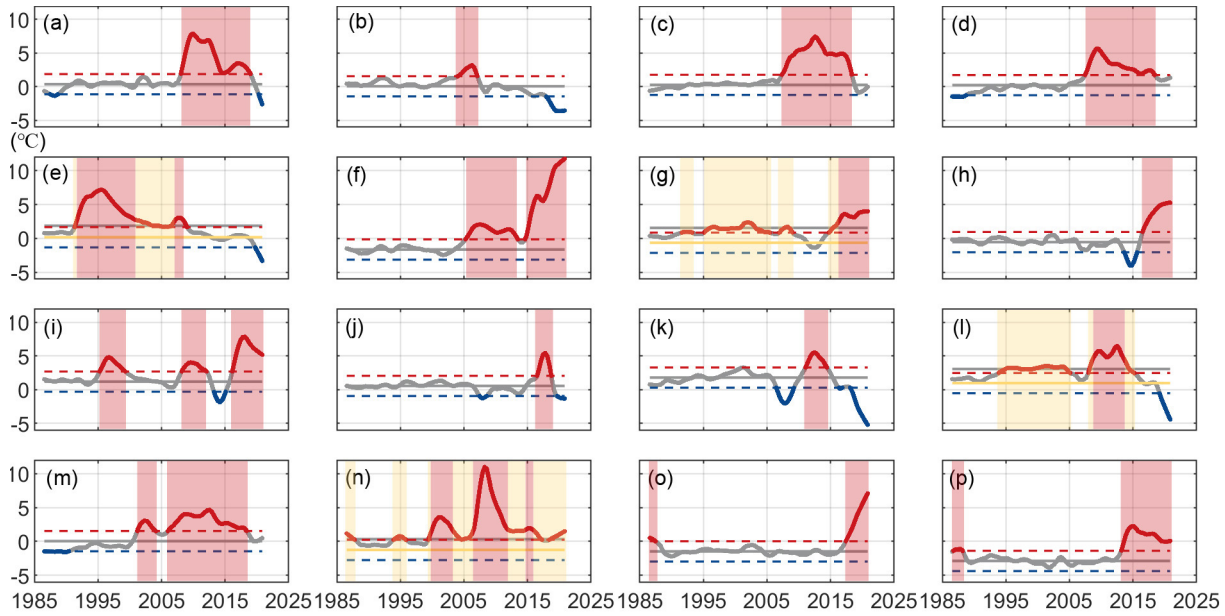

Fig. 7. Trend components of LST time series in the locations of ground points GP1–GP16. The gray horizontal lines represent the fit lines from the RANSAC algorithm, indicating the initial background LST values. The yellow horizontal lines are the new background LST values lines after the calibration of the fit lines with the field surveys (calculated in Section IV-C). The red and blue dashed lines are the lines with values 1.5 °C above and 1.5 °C below the calibrated background LST values lines [in subfigures (e), (g), (l), and (n)] or the initial background LST values lines [in subfigures (a)–(d), (f), (h)–(k), (m), (o), and (p)]. (a) GP1. (b) GP2. (c) GP3. (d) GP4. (e) GP5. (f) GP6. (g) GP7. (h) GP8. (i) GP9. (j) GP10. (k) GP11. (l) GP12. (m) GP13. (n) GP14. (o) GP15. (p) GP16.

TABLE I

COAL FIRE BURNING INFORMATION OF GROUND POINTS GP1–GP16 INVESTIGATED FROM THIS STUDY (BEFORE "/") AND OBTAINED FROM FIELD SURVEYS IN NINE YEARS FROM 2002 TO 2018 AND FROM THE RAE METHOD IN 2014 (AFTER "/")

Ground points	2002	2003	2004	2005	2006	2008	2010	2014	2018
GP1	no / no	no / no	no / no	no / no	no / no	no / no	fire / fire	fire / -	fire / -
GP2	no / no	no / fire	no / no	fire / fire	fire / fire	no / no	no / no	no / -	no / -
GP3	no / no	no / no	no / no	no / no	no / no	no / no	fire / no	fire / fire	no / -
GP4	no / no	no / fire	no / no	no / fire	no / fire	fire / fire	fire / no	fire / -	fire / -
GP5	fire / fire	no / fire	no / fire	no / fire	no / fire	no / no	no / no	no / -	no / -
GP6	no / no	no / no	no / no	no / no	fire / fire	fire / fire	fire / fire	fire / -	fire / -
GP7	no / fire	no / no	no / fire	no / fire	no / fire	no / no	no / no	fire / fire	fire / -
GP8	no / no	no / no	no / no	no / no	no / no	no / no	no / no	no / -	fire / fire
GP9	no / no	no / no	no / no	no / no	no / no	no / no	fire / no	no / fire	fire / -
GP10	no / no	no / fire	no / no	no / no	no / no	no / no	no / no	no / fire	fire / -
GP11	fire / no	no / no	no / no	no / no	no / no	no / no	no / no	fire / fire	no / -
GP12	no / fire	no / fire	no / fire	no / fire	no / fire	no / fire	fire / no	no / -	no / fire
GP13	no / fire	fire / fire	fire / fire	fire / fire	fire / fire	fire / fire	fire / fire	fire / fire	fire / -
GP14	fire / fire	fire / fire	fire / fire	no / fire	fire / fire	fire / fire	fire / fire	fire / -	no / -
GP15	no / no	no / no	no / no	no / no	no / no	no / no	no / fire	no / -	fire / -
GP16	no / no	no / no	no / no	no / no	no / no	no / no	no / no	fire / fire	fire / -

C. Spatiotemporal Dynamics Model of Coal Fires

1) Developing Spatiotemporal 3-D Coal Fire Model: For all pixels in the coal fire areas from 1986 to 2020, the RANSAC algorithm was performed for judging the burning period. The judgment was visualized in a spatiotemporal 3-D (longitude, latitude, and time) model in Fig. 9(a) and (b) with pixels sparsely sampled in a 5 × 5 pixels window. The red color represents that the LST values were at least 1.5 °C greater than the background LST values, indicating a burning coal fire; the blue color shows that the LST values were at least 1.5 °C lower than the background LST values, suggesting low temperature in that period.

From the above analysis, the bar with much blue color but a little red color should be paid more attention to because of the inaccuracy of the RANSAC estimation affected by a large number of outliers, i.e., coal fire burning for a long period. To evaluate the accuracy of the identification of the coal fire burning period from the RANSAC algorithm, the SAX algorithm was applied to the trend components of these coal fire pixels. The values of the trend components were classified into four sections, with values from low to high symbolized by "low," "medium low," "medium high," and "high." Fig. 9(c) shows the symbol that the fit line of each pixel belongs to. Pixels labeled with the symbol "low" mean that the fit line of that pixel is in the lowest section of the trend component time series, indicating that the outliers are higher than the fit line. This is true for coal fire identification because coal fire temperatures are higher than background

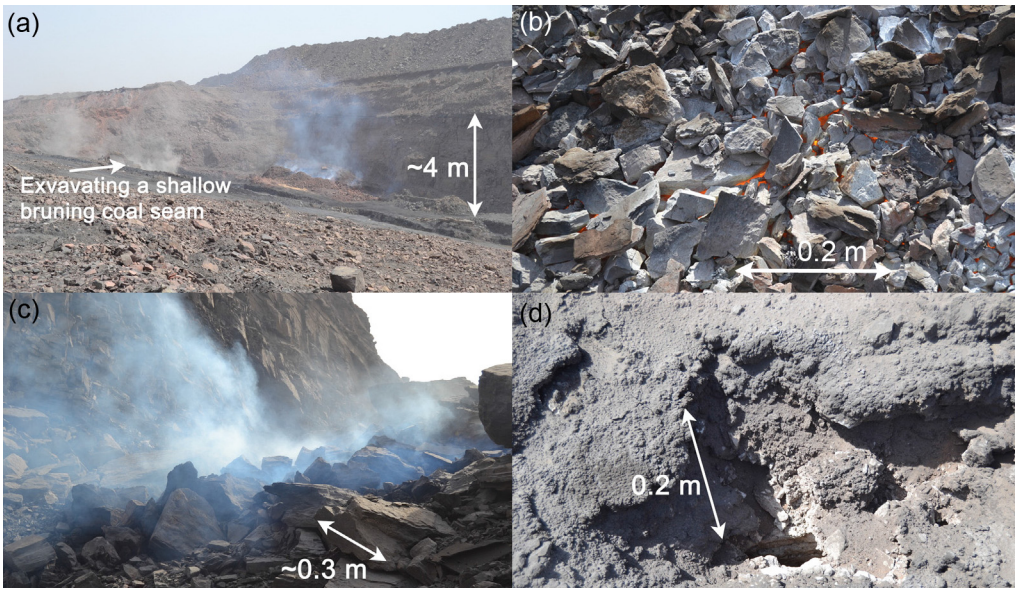

Fig. 8. Observed (a) shallow burning coal seam located in ground point GP7, (b) burning coal waste pile located in GP9, (c) smoke emitting from rock lumps located in GP10, and (d) vent located in GP13 in the 2014 *in situ* field campaign. (Photograph by Zeyang Song in 2014, modified from [42]).

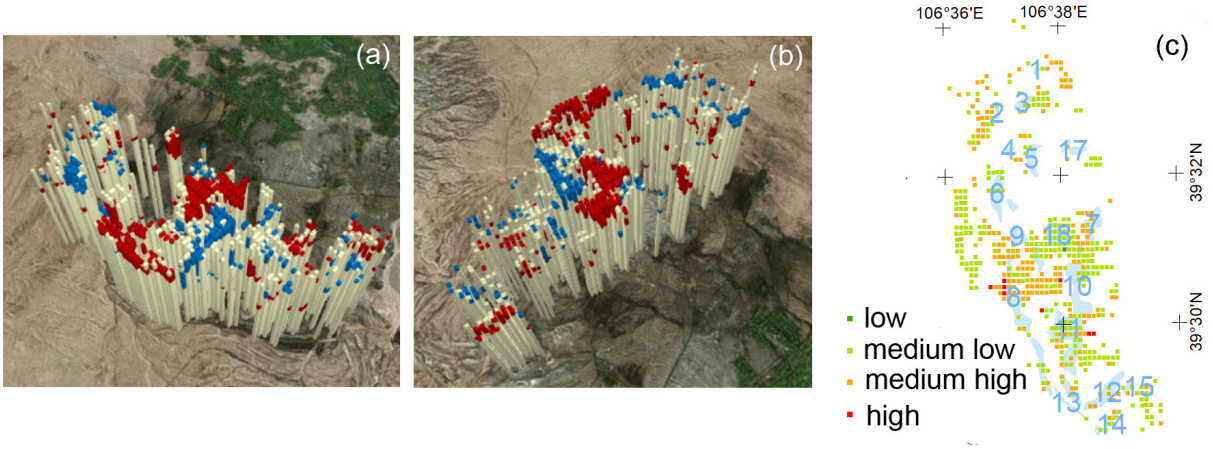

Fig. 9. (a) and (b) Coal fire dynamics before calibration. The bar from the bottom to the top indicates the period from 1986 to 2020. The red color indicates that, in that period, the LST values were at least 1.5 °C greater than the background LST values; the blue color indicates that, in that period, the LST values were at least 1.5 °C lower than the background LST values. (c) Symbols that the fit lines belong to in the range of the trend components.

temperatures. Therefore, the detection of coal fire dynamics at pixels with the symbol "low" can be regarded as accurate and robust. The detection at pixels labeled with the symbol "medium low" is a little worse than "low," followed by those at pixels labeled with the symbol "medium high." The detection of pixels labeled with the symbol "high" means that the fit line is on the top section of the trend components time series. It is the worst case because the outliers are below the fit line, and consequently, no coal fire was detected in this case. This is possible because of the long period of coal fire burning causing large numbers of high LST values. Therefore, the fit line needs to be calibrated to adapt to the actual cases according to the field survey, to track the actual spatiotemporal characters of the coal fire dynamics, and further to provide modified standard background LST values for the future monitoring of the fire.

2) Calibration Using Field Surveys in 2002–2005: The coal fire zones delineated from field surveys in 2002–2005 were employed for the calibration of the fit lines from the RANSAC algorithm. The coal fire zones in the 2006–2010 field surveys, the hot spots in 2018, and the new coal fire zones detected by the RAE method in 2014 were used for validation. For the calibration, first, the numbers of burning years of each point from the filed surveys in 2002–2005 were counted. Taking GP1–GP5 as an example, those numbers are 0, 2, 0, 2, and 4 (see columns 2–5 in Table I). This number of years is set as a threshold for each point. If burning information extracted from this study and the field surveys have biases less than the thresholds, their fit lines from the RANSAC algorithm were kept. Otherwise, the fit lines were iteratively shifted down with a step of 0.1 until the biases meet the thresholds. Here, the thresholds for the ground points GP5, GP7, GP12,

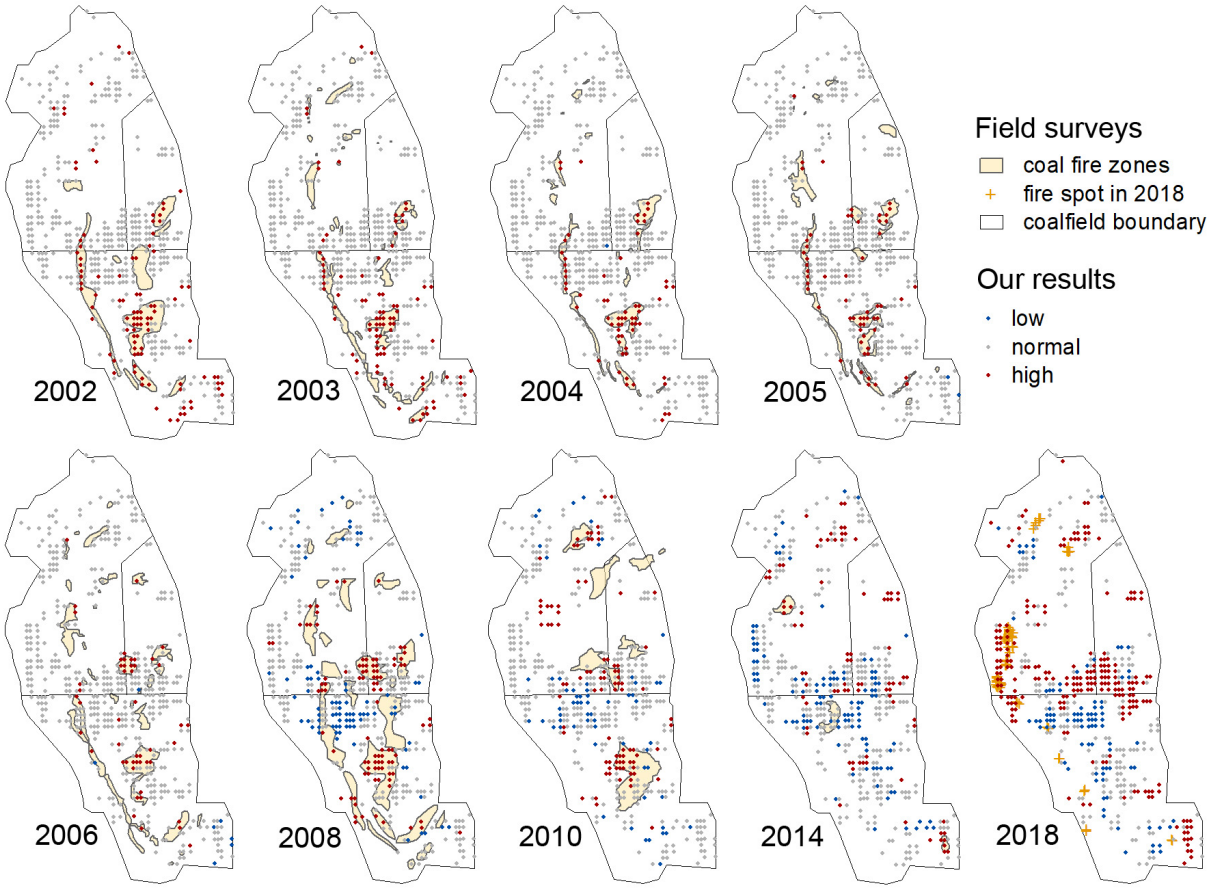

Fig. 10. Calibrated low, background, and high values from this study and the coal fire zones from field surveys in the years 2002–2010 and 2018, and the RAE method in the year 2014. Field survey data in 2002–2005 were used for calibration. Field survey data in 2006–2010 and 2018, and the RAE result in 2014 were used for validation. Red pixels are highly associated with coal fire areas.

and GP14 were four, three, four, and four years. However, they were detected with only one-, one-, zero-, and three-year consistencies with the field survey. The fit lines were iteratively shifted down by a step of 0.1 until the consistency reaches the thresholds. The calibrated fit lines were the yellow horizontal lines shown in Fig. 7(e), (g), (l), and (n). The calibration process was also taken to all the coal fire pixels.

3) Validation With Field Surveys and RAE Method: The calibrated coal fire dynamics for all the coal fire pixels in the years when there was field survey data or RAE result were shown in Fig. 10, overlaid with coal fire zones or hot spots from field surveys or the RAE method. Statistics were made to show the consistency between the detected high-temperature values and the coal fire zones from the field surveys. In each coal fire zone, if the number of high-value (red) pixels is more than that of background/low value (gray/blue) pixels, the coal fire zone is recognized as the high-value zone. If those numbers are equal or there was no pixel inside that coal fire zone, the zone will be excluded from the statistic. The number of high-value zones in the year 2002 accounts for 5/8 of the coal fire zones, which means that 62.5% of the coal fire zones were recognized as high-value zones by the proposed method. The percentages for the recognized high-value zones are 53.3% in the year 2003, 66.7% in 2004, 85.7% in 2005, 26.7% in 2006, 50% in 2008, 50% in 2010, and 66.7% in 2014. Although the percentage is not so high, the spatial distribution of the recognized high-value zones is consistent with the spatial distribution of zones from field surveys. In the years 2002–2005, whose field survey data were used for the calibration, the estimated coal fire pixels showed very high consistency with the field surveys, with more than 50% of high-value zones. For the years 2006, 2008, and 2010, which work as validation data, the coal fire areas were not so consistent with 50% or less than 50% of high-value zones, but the spatial distribution was very close. In the year 2018, the high-value zones were consistent with the field surveys in the edge area without opencast blasting and excavating mining activities [39]. Two of the three new coal fire zones in 2014 detected by the RAE method were completely in agreement with the high values from this study. The validation confirmed that most of the high values in the years 2002–2010 and 2014 and in the edges areas in 2018 were coal fires.

4) Spatiotemporal 3-D Coal Fire Model: After the calibration, the spatiotemporal 3-D coal fire model was shown in Fig. 11, which presented more complex and detailed coal fire dynamics. In the north part of the coalfield around the coal fire zone 1, there were some high LST values in the past, but, now, they are background values or low values. It indicates that, in the past, this area has experienced coal fires, but, now, the fire is distinct, which is true compared with the field surveys.

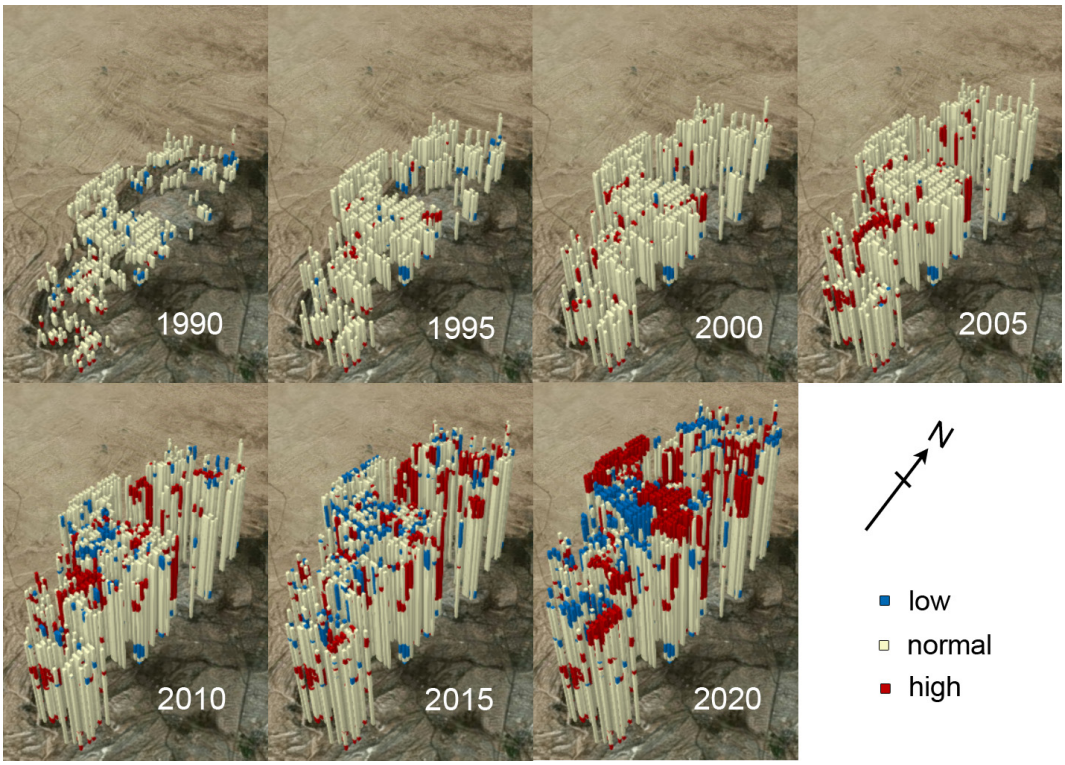

Fig. 11. Spatiotemporal evolution of coal fires in the Wuda coalfield. Red pixels indicating high LST values have a great possibility to be coal fires.

In the west part of the coalfield close to the coal fire zones 6 and 9, the areas were in background LST values in the early years but in high values within the recent five years, indicating that they are newly ignited fires. This situation is similar to the ground points GP18, which were detected to be the hot spot in the field survey in the year 2018 (see Fig. 10), but no coal fire in the period 2002–2010. In the center of the coalfield, one part around the coal fire zone 18 is in red, which means that they are in high values in the current period, but the actual situation cannot be determined because of the opencast blasting and excavating mining activities [39]. The area between the coal fire zones 8 and 10 is in blue in the top part of the bars, which means that they are in low values in the current period, but, before the calibration, in the early period, it did not show any red color. This is not the same as the field surveys because there were fires in the past. After the calibration of the fit lines according to the fieldwork, the situation changes, which is very similar to the ground points GP11 and GP12.

This spatiotemporal 3-D model also makes the monitoring of coal fire spatial propagation possible. High-resolution long-term coal fire burning stages provide a more detailed coal fire propagation in the spatial domain. The temporal coal fire dynamics in the study area show an evident spatial correlation inside each coal fire zone. At the beginning of the study period, from 1986 to 1990, there were just a few coal fire areas in the south. In the years 1990–1995, a coal fire area appeared in the east and several very small coal fire areas appeared in the south. In 1995–2000, the coal fire areas expanded, and in 2000–2005, the coal fire areas were larger. In 2005–2010, the coal fire areas became larger than before, and there was a large coal fire area in the south. Some low LST values were appeared in this period possibly because of the fire-fighting activities, e.g., spraying of water. In 2010–2015, the coal fire areas were decreased, and low values were increased, indicating the conduction of fire-fighting activities. Coal fires were mainly located in the north in that period. In 2015–2020, there were large areas of low values, but also large areas of high values appeared as several clusters. Near the edge of the coalfield, especially in the western part, the high values are validated to be coal fire spots in 2018, but, in the center of the coalfield, the high values were not validated because of the opencast blasting and excavating mining activities there.

From the geological and geomorphological point of view, the longwall mining, depth of coal seam, overlying rock properties, and geological fault were significant factors for the coal fire dynamics. Seven boreholes were drilled during the geological surveys [61]. In the north part of Huangbaici Coal Mine, the rare coal fires could be due to the deeper coal seam and stiff overlying rocks. In the Suhaitu Coal Mine, most of the coal fires were triggered by longwall mining activities [61]. In the south of the coal fire zones 2 and 3, extracted coal seam formed a caved zone, i.e., overlying rocks collapse, leading to subsidence. When the depth of extracted coal seam is shallow, cracks and fissures were generated. The main overlying rock layers in that area consisted of shales, which were prone to mechanical failure. Fieldwork confirmed that the ventilation pathways existed in the coal fire zones. Around coal fire zone 3, several faults existed [61] with cracks confirmed by the field surveys [62], promoting coal fire propagation. It could be the possible explanation for more coal fires appearing

in zone 3 after 2010. In zone 8, the coal fire was mainly associated with outcrops of the coal seam. The fire had been burning for a long period before 2005, but it was not so evident after 2006. Coal fire in zone 11 was caused by private mining activities, which seems decreased significantly after the year 2010, possibly due to the fire-fighting activities.

V. Discussion

Coal fires are extremely complex, unpredictable, and uncontrollable processes, influenced by geological conditions, climate environment, and human activity. The proposed methodology has some merits in monitoring coal fire dynamics. First, it improves the accuracy of identifying coal fire in the temporal domain. The long-term time series analysis of LST in pixel scale can mitigate the influence of land geological condition, land use, and the atmospheric effect on Landsat images. Time series decomposition can capture the trend, remove the seasonality, and leave out the noise. The application of the RANSAC algorithm detects the coal fire burning period and, thus, implements the identification of the persistent coal fire. Besides, the proposed methodology facilitates the analysis of coal fire dynamics in the spatial domain. Long-term high-resolution LST time series presents the coal fire burning stages and provides a more detailed coal fire propagation with a more accurate time compared with the discrete LST data. Furthermore, the proposed methodology can also be applied for a current coal fire detection synchronized with image acquisitions. At each pixel, the background (or the calibrated background) LST value can be predicted by adding the decomposed seasonal component to the fit line [63]. When the new image is acquired, the two LST values can be compared. If the LST calculated from Landsat images is much higher than the predicted one, the pixel has a large possibility to be a coal fire pixel.

LST is a key variable for climate and ecological environment research. The spatial and temporal variabilities of LST are significant in understanding the natural and anthropogenic phenomena and processes on the land surface [64], [65]. The proposed methodology might be applied to estimate these long-term changes of the land surface, e.g., geothermal anomalous changes [57], [66], volcanic activities [67], glaciers melting [68], and permafrost thawing [69]. The proposed methodology can also be applied to other seasonal remote sensing data or products, e.g., normalized difference vegetation index and land surface deformation.

There are assumptions, limitations, or delimitations in this study. First, for the data resources and data preprocessing, only daytime TIR data from Landsat and only statistical monowindow algorithms were employed. The gaps on Landsat 7 data, and the image striping and image banding on Landsat 8 TIRS data may affect the results of this study. Second, the results from the RANSAC algorithm show some inaccuracy in some areas because of the shifted fit line, possibly caused by the number of inliers less than 50%. The representative areas are the areas surrounding GP5, GP7, GP12, and GP14. In this case, it means that the areas suffer coal fire burning for a long time. Although the fit lines have been calibrated with the field surveys, the calibration also has some uncertainty due to the limited field surveys. Finally, the threshold, i.e., ± 1.5 °C, for judging the coal fire period is determined based on the statistics of the LST values in the background areas without considering the characteristics of the land.

In future study, first, higher quality data and more advanced algorithms can be employed to improve the capability in identifying the thermal anomalies. Data can be a higher spatial resolution (e.g., unmanned aerial vehicle) [13] data, more nighttime Landsat or ASTER images, and more auxiliary, e.g., geological, geomorphological, and meteorological data. Algorithms include more accurate TIR calibration methods [35], [43], [44], more efficient LST retrieval algorithms [70], and fusion algorithms on data with different spatial resolution or with different time (daytime or nighttime) or from different sensors [71], [72]. Second, the shift of the fit line from RANSAC can be fixed by considering more field surveys or trying optimal RANSAC [73]. The thresholds for judging the coal fire burning period can be modified based on the characteristic of land in each pixel and the field surveys. Once the background values and the threshold for the burning stages are determined, the coal fire situation will be clearer. Moreover, auxiliary data, such as meteorological parameters and coal geology, can be collected to understand the persistent coal fire dynamics and develop strategies to prevent coal fire hazards.

VI. Conclusion

In this study, a comprehensive methodology for monitoring persistent coal fires was proposed. Time series decomposition and analysis were applied to the pixelwise LST derived from 35 years' Landsat images for monitoring the long-term persistent coal fire dynamics. Coal fire areas were identified by the statistical information of the decomposed LST trend components. The gradual and abrupt LST changes were detected by the Mann–Kendall and the Pettitt tests, showing the possible evolution of the coal fire burning stages. The RANSAC and the SAX algorithms were applied to trend components vectors to judge the coal fire burning period and evaluate the robustness of the results. Calibration was conducted according to the filed surveys, obtaining a spatiotemporal 3-D diagram showing both spatial and temporal coal fire dynamics in the Wuda coalfield from 1986 to 2020. The achieved results were well-matched with the field surveys in 2002–2010 and 2018, and with the RAE result in 2014, proving the validity and feasibility of the proposed methodology. The methodology fully excavates the capability of the long-term remote sensing data and employed them to a persistent and dangerous hazard with great performance. This study can provide a scientific basis for the prevention and mitigation of coal fire hazards and further protect the resources and environments. In future studies, more auxiliary data, such as field surveys, and geological and meteorological data, can be collected to understand the coal fire phenomenon and improve the accuracy of coal fire monitoring.

Acknowledgment

Landsat data courtesy of the U.S. Geological Survey. The authors would like to thank the anonymous referees for

the constructive comments and suggestions. The author Xue Chen would like to thank M. Floris, F. Catani, C. Sun, and S. Puliero for the caring and sharing in Padova.

REFERENCES

[1] G. B. Stracher, "Coal fires burning around the world: A global catastrophe," *Int. J. Coal Geol.*, vol. 59, nos. 1–2, pp. 1–6, Jul. 2004, doi: 10.1016/j.coal.2004.01.001.

[2] J. Zhang, C. Kuenzer, A. Tetzlaff, D. Oertel, B. Zhukov, and W. Wagner, "Thermal characteristics of coal fires 2: Results of measurements on simulated coal fires," *J. Appl. Geophys.*, vol. 63, nos. 3–4, pp. 135–147, Dec. 2007, doi: 10.1016/j.jappgeo.2007.08.003.

[3] C. Kuenzer and S. Dech, "Thermal infrared remote sensing of surface and underground coal fires," *Thermal Infrared Remote Sens.*, vol. 17, pp. 453–473, Jul. 2013, doi: 10.1007/978-94-007-6639-6.

[4] Z. Song and C. Kuenzer, "Coal fires in China over the last decade: A comprehensive review," *Int. J. Coal Geol.*, vol. 133, pp. 72–99, Nov. 2014, doi: 10.1016/j.coal.2014.09.004.

[5] T. H. Syed, M. J. Riyas, and C. Kuenzer, "Remote sensing of coal fires in India: A review," *Earth-Sci. Rev.*, vol. 187, pp. 338–355, Dec. 2018, doi: 10.1016/j.earscirev.2018.10.009.

[6] R. S. Gautam, D. Singh, A. Mittal, and P. Sajin, "Application of SVM on satellite images to detect hotspots in Jharia coal field region of India," *Adv. Space Res.*, vol. 41, no. 11, pp. 1784–1792, Jan. 2008, doi: 10.1016/j.asr.2007.05.011.

[7] S. T. Ide and F. M. Orr, "Comparison of methods to estimate the rate of CO_2 emissions and coal consumption from a coal fire near Durango, CO," *Int. J. Coal Geol.*, vol. 86, no. 1, pp. 95–107, Apr. 2011, doi: 10.1016/j.coal.2010.12.005.

[8] C. D. Ellyett and A. W. Fleming, "Thermal infrared imagery of the Burning Mountain coal fire," *Remote Sens. Environ.*, vol. 3, no. 1, pp. 79–86, Jan. 1974, doi: 10.1016/0034-4257(74)90040-6.

[9] G. Schaumann, B. Siemon, and Y. Changchun, "Geophysical investigation of Wuda coal mining area, inner Mongolia: Electromagnetics and magnetics for coal fire detection," in *Spontaneous Coal Seam Fires: Mitigating a Global Disaster. International Research for Sustainable Control and Management* (ERSEC Ecological Book Series). Beijing, China: Tsinghua Univ. Press, 2008, pp. 336–350, doi: 10.2314/GBV:545690129.

[10] M. O. B. Rúa, A. J. D. Aragón, and P. B. Baena, "A study of fire propagation in coal seam with numerical simulation of heat transfer and chemical reaction rate in mining field," *Int. J. Mining Sci. Technol.*, vol. 29, no. 6, pp. 873–879, Dec. 2019, doi: 10.1016/j.ijmst.2019.09.003.

[11] A. Rosema *et al.*, *Manual of Coal Fire Detection and Monitoring: Report of the Project: Development and Implementation of a Coal Fire Monitoring and Fighting System in China*. Delft, The Netherlands: The Netherlands Institute of Applied Geoscience (NITG), 1999.

[12] J. Zhang, "Spatial and statistical analysis of thermal satellite imagery for extraction of coal fire related anomalies," Ph.D. dissertation, Vienna Univ. Technol., Vienna, Austria, 2004.

[13] X. He, X. Yang, Z. Luo, and T. Guan, "Application of unmanned aerial vehicle (UAV) thermal infrared remote sensing to identify coal fires in the Huojitu coal mine in Shenmu city, China," *Sci. Rep.*, vol. 10, no. 1, pp. 1–13, Dec. 2020, doi: 10.1038/s41598-020-70964-5.

[14] W. Zhengming and J. Dozier, "Land-surface temperature measurement from space: Physical principles and inverse modeling," *IEEE Trans. Geosci. Remote Sens.*, vol. 27, no. 3, pp. 268–278, May 1989, doi: 10.1109/36.17668.

[15] Q. Weng, "Thermal infrared remote sensing for urban climate and environmental studies: Methods, applications, and trends," *ISPRS J. Photogramm. Remote Sens.*, vol. 64, no. 4, pp. 335–344, Jul. 2009, doi: 10.1016/j.isprsjprs.2009.03.007.

[16] S. Kaya and U. M. Leloglu, "Buried and surface mine detection from thermal image time series," *IEEE J. Sel. Topics Appl. Earth Observ. Remote Sens.*, vol. 10, no. 10, pp. 4544–4552, Oct. 2017, doi: 10.1109/JSTARS.2016.2639037.

[17] C. Ru *et al.*, "Land surface temperature retrieval from Landsat 8 thermal infrared data over urban areas considering geometry effect: Method and application," *IEEE Trans. Geosci. Remote Sens.*, vol. 60, Jun. 2021, Art. no. 5000716, doi: 10.1109/TGRS.2021.3088482.

[18] V. Karanam, M. Motagh, S. Garg, and K. Jain, "Multi-sensor remote sensing analysis of coal fire induced land subsidence in Jharia coalfields, jharkhand, India," *Int. J. Appl. Earth Observ. Geoinf.*, vol. 102, Oct. 2021, Art. no. 102439.

[19] A. Prakash, R. P. Gupta, and A. K. Saraf, "A landsat TM based comparative study of surface and subsurface fires in the Jharia coalfield, India," *Int. J. Remote Sens.*, vol. 18, no. 11, pp. 2463–2469, Jul. 1997, doi: 10.1080/014311697217738.

[20] A. Raju, R. P. Gupta, and A. Prakash, "Delineation of coalfield surface fires by thresholding landsat TM-7 day-time image data," *Geocarto Int.*, vol. 28, no. 4, pp. 343–363, Jul. 2013, doi: 10.1080/10106049.2012.710651.

[21] A. K. Saraf, A. Prakash, S. Sengupta, and R. P. Gupta, "Landsat-TM data for estimating ground temperature and depth of subsurface coal fire in the Jharia coalfield, India," *Int. J. Remote Sens.*, vol. 16, no. 12, pp. 2111–2124, Aug. 1995, doi: 10.1080/01431169508954545.

[22] C. Kuenzer, J. Zhang, J. Li, S. Voigt, H. Mehl, and W. Wagner, "Detecting unknown coal fires: Synergy of automated coal fire risk area delineation and improved thermal anomaly extraction," *Int. J. Remote Sens.*, vol. 28, no. 20, pp. 4561–4585, Oct. 2007, doi: 10.1080/01431160701250432.

[23] X. Du, D. Cao, D. Mishra, S. Bernardes, T. Jordan, and M. Madden, "Self-adaptive gradient-based thresholding method for coal fire detection using ASTER thermal infrared data, Part I: Methodology and decadal change detection," *Remote Sens.*, vol. 7, no. 6, pp. 6576–6610, May 2015, doi: 10.3390/rs70606576.

[24] H. Huo *et al.*, "A study of coal fire propagation with remotely sensed thermal infrared data," *Remote Sens.*, vol. 7, no. 3, pp. 3088–3113, Mar. 2015, doi: 10.3390/rs70303088.

[25] T. D. Vu and T. T. Nguyen, "Spatio-temporal changes of underground coal fires during 2008–2016 in Khanh Hoa coal field (North-east of Viet Nam) using landsat time-series data," *J. Mountain Sci.*, vol. 15, no. 12, pp. 2703–2720, Dec. 2018, doi: 10.1007/s11629-018-4997-z.

[26] P. Sismanidis, B. Bechtel, I. Keramitsoglou, and C. T. Kiranoudis, "Mapping the spatiotemporal dynamics of Europe's land surface temperatures," *IEEE Geosci. Remote Sens. Lett.*, vol. 15, no. 2, pp. 202–206, Feb. 2018, doi: 10.1109/LGRS.2017.2779829.

[27] J. Pandey, D. Kumar, D. C. Panigrahi, and V. K. Singh, "Temporal transition analysis of coal mine fire of Jharia coalfield, india, using landsat satellite imageries," *Environ. Earth Sci.*, vol. 76, no. 12, pp. 1–13, Jun. 2017, doi: 10.1007/s12665-017-6765-8.

[28] W. Jiang, K. Jia, Z. Chen, Y. Deng, and P. Rao, "Using spatiotemporal remote sensing data to assess the status and effectiveness of the underground coal fire suppression efforts during 2000–2015 in Wuda, China," *J. Cleaner Prod.*, vol. 142, pp. 565–577, Jan. 2017, doi: 10.1016/j.jclepro.2016.03.082.

[29] R. K. Mishra, J. K. Pandey, J. Pandey, S. Kumar, and P. N. S. Roy, "Detection and analysis of coal fire in Jharia coalfield (JCF) using landsat remote sensing data," *J. Indian Soc. Remote Sens.*, vol. 48, no. 2, pp. 181–195, Feb. 2020, doi: 10.1007/s12524-019-01067-6.

[30] R. Mujawdiya, R. S. Chatterjee, and D. Kumar, "MODIS land surface temperature time series decomposition for detecting and characterizing temporal intensity variations of coal fire induced thermal anomalies in Jharia coalfield, India," *Geocarto Int.*, pp. 1–15, Sep. 2020, doi: 10.1080/10106049.2020.1818853.

[31] H. B. Mann, "Nonparametric tests against trend," *Econometrica*, vol. 13, no. 3, pp. 245–259, Jan. 1945. [Online]. Available: http://www.jstor.com/stable/1907187

[32] M. G. Kendall, *Rank Correlation Methods*, 4th ed. London, U.K.: Griffin, 1975.

[33] A. N. Pettitt, "A non-parametric approach to the change-point problem," *J. Roy. Stat. Soc. C*, vol. 28, no. 2, pp. 126–135, 1979, doi: 10.2307/2346729.

[34] M. A. Fischler and R. Bolles, "Random sample consensus: A paradigm for model fitting with applications to image analysis and automated cartography," *Commun. ACM*, vol. 24, no. 6, pp. 381–395, 1981.

[35] J. A. Barsi *et al.*, "Landsat-8 TIRS thermal radiometric calibration status," *Proc. SPIE*, vol. 10402, Sep. 2017, Art. no. 104021G, doi: 10.1117/12.2276045.

[36] L. Jiang, H. Lin, J. Ma, B. Kong, and Y. Wang, "Potential of small-baseline SAR interferometry for monitoring land subsidence related to underground coal fires: Wuda (Northern China) case study," *Remote Sens. Environ.*, vol. 115, no. 2, pp. 257–268, Feb. 2011, doi: 10.1016/j.rse.2010.08.008.

[37] A. Tetzlaff, "Coal fire quantification using ASTER, ETM and BIRD satellite instrument data," Ph.D. dissertation, LMU, Munich, Germany, 2004, doi: 10.5282/edoc.4398.

[38] Z. Song and C. Kuenzer, "Spectral reflectance (400–2500 nm) properties of coals, adjacent sediments, metamorphic and pyrometamorphic rocks in coal-fire areas: A case study of Wuda coalfield and its surrounding areas, northern China," *Int. J. Coal Geol.*, vol. 171, pp. 142–152, Feb. 2017, doi: 10.1016/j.coal.2017.01.008.

[39] F. Li, J. Li, X. Liu, and X. Meng, "Coal fire detection and evolution of trend analysis based on CBERS-04 thermal infrared imagery," *Environ. Earth Sci.*, vol. 79, no. 16, pp. 1–15, Aug. 2020, doi: 10.1007/s12665-020-09125-w.
[40] S. Dai, D. Ren, Y. Tang, L. Shao, and S. Li, "Distribution, isotopic variation and origin of sulfur in coals in the Wuda coalfield, Inner Mongolia, China," *Int. J. Coal Geol.*, vol. 51, no. 4, pp. 237–250, 2002, doi: 10.1016/S0166-5162(02)00098-8.
[41] C. Kuenzer, J. Zhang, Y. Sun, Y. Jia, and S. Dech, "Coal fires revisited: The Wuda coal field in the aftermath of extensive coal fire research and accelerating extinguishing activities," *Int. J. Coal Geol.*, vol. 102, pp. 75–86, Nov. 2012, doi: 10.1016/j.coal.2012.07.006.
[42] Z. Song *et al.*, "Analysis of coal fire dynamics in the Wuda syncline impacted by fire-fighting activities based on *in-situ* observations and Landsat-8 remote sensing data," *Int. J. Coal Geol.*, vols. 141–142, pp. 91–102, Mar. 2015, doi: 10.1016/j.coal.2015.03.008.
[43] M. Montanaro, A. Gerace, A. Lunsford, and D. Reuter, "Stray light artifacts in imagery from the Landsat 8 thermal infrared sensor," *Remote Sens.*, vol. 6, no. 11, pp. 10435–10456, Oct. 2014, doi: 10.3390/rs61110435.
[44] United States Geological Survey. (2019). *Landsat 8 OLI and TIRS Calibration Notices*. Accessed: Nov. 27, 2021. [Online]. Available: https://www.usgs.gov/core-science-systems/nli/landsat/landsat-8-oli-and-tirs-calibration-notices
[45] S. L. Ermida, P. Soares, V. Mantas, F. M. Göttsche, and I. F. Trigo, "Google earth engine open-source code for land surface temperature estimation from the Landsat series," *Remote Sens.*, vol. 12, no. 9, pp. 1–21, 2020, doi: 10.3390/RS12091471.
[46] R. B. Cleveland, E. S. Cleveland, J. E. McRae, and I. Terpernning. (1990). *STL: A Seasonal-Trend Decomposition Procedure Based on Loess*. [Online]. Available: https://www.ncbi.nlm.nih.gov/pubmed/2207653
[47] V. C. F. Gomes, G. R. Queiroz, and K. R. Ferreira, "An overview of platforms for big Earth observation data management and analysis," *Remote Sens.*, vol. 12, no. 8, pp. 1–25, 2020, doi: 10.3390/RS12081253.
[48] A. Duguay-Tetzlaff *et al.*, "Meteosat land surface temperature climate data record: Achievable accuracy and potential uncertainties," *Remote Sens.*, vol. 7, pp. 13139–13156, 2015.
[49] R. J. Hyndman and G. Athanasopoulos, "Forecasting: Principles and practice," in *Principles of Optimal Design*. OTexts, 2018, p. 504. [Online]. Available: https://otexts.com/fpp2/
[50] R Core Team. (2018). *R: A Language and Environment for Statistical Computing*. Vienna, Austria. [Online]. Available: https://www.r-project.org/
[51] G. Van Rossum and F. L. Drake, Jr., *Python Tutorial*. Amsterdam, The Netherlands: Centrum voor Wiskunde en Informatica, 1995.
[52] M. M. H. Shourov, I. Mahmud, and K. Niemeyer, *mmhs013/pyMannKendall: V1.4.2*. Zenodo, May 2021. [Online]. Available: https://zenodo.org/record/4849563#.YeyURv5BxPY, doi: 10.5281/zenodo.4849563.
[53] K. G. Derpanis, "Overview of the RANSAC algorithm," *Image Rochester NY*, vol. 4, no. 1, pp. 2–3, 2010, doi: 10.1002/cne.901000107.
[54] A. Nurunnabi, D. Belton, and G. West, "Robust segmentation for large volumes of laser scanning three-dimensional point cloud data," *IEEE Trans. Geosci. Remote Sens.*, vol. 54, no. 8, pp. 4790–4805, Aug. 2016, doi: 10.1109/TGRS.2016.2551546.
[55] *9.7.0.1190202 (R2019b)*, MATLAB, The MathWorks Inc., Natick, MA, USA, 2018.
[56] G. Yan, "Pixel based and object oriented image analysis for coal fire research," M.S. thesis, ITC, Univ. Twente, Enschede, The Netherlands, Tech. Rep., 2003.
[57] Y. Yan *et al.*, "Driving forces of land surface temperature anomalous changes in North America in 2002–2018," *Sci. Rep.*, vol. 10, no. 1, pp. 1–13, Dec. 2020, doi: 10.1038/s41598-020-63701-5.
[58] V. Satopää, J. Albrecht, D. Irwin, and B. Raghavan, "Finding a," kneedle" in a haystack: Detecting knee points in system behavior," in *Proc. Int. Conf. Distrib. Comput. Syst.*, 2011, pp. 166–171, doi: 10.1109/ICDCSW.2011.20.
[59] B. Eli. (2012). *Peakdet: Peak Detection Using MATLAB*. [Online]. Available: https://billauer.co.il/peakdet.html
[60] M. Forkel, N. Carvalhais, J. Verbesselt, M. D. Mahecha, C. S. R. Neigh, and M. Reichstein, "Trend Change detection in NDVI time series: Effects of inter-annual variability and methodology," *Remote Sens.*, vol. 5, no. 5, pp. 2113–2144, Apr. 2013, doi: 10.3390/rs5052113.
[61] Z. Song, Z. Yu, J. Zhao, M. Li, and J. Deng, "Bow-tie analysis of underground coal-fire hazards and mining activities using hybrid data: A case study of Wuda coalfield in inner Mongolia, China," in *Bow Ties in Process Safety and Environmental Management*. Boca Raton, FL, USA: CRC Press, 2022, pp. 31–44.
[62] C. Kuenzer and G. B. Stracher, "Geomorphology of coal seam fires," *Geomorphology*, vol. 138, pp. 209–222, Feb. 2012.
[63] A. Mathew, S. Sreekumar, S. Khandelwal, N. Kaul, and R. Kumar, "Prediction of land-surface temperatures of jaipur city using linear time series model," *IEEE J. Sel. Topics Appl. Earth Observ. Remote Sens.*, vol. 9, no. 8, pp. 3546–3552, Aug. 2016, doi: 10.1109/JSTARS.2016.2523552.
[64] P. Fu and Q. Weng, "Temporal dynamics of land surface temperature from Landsat TIR time series images," *IEEE Geosci. Remote Sens. Lett.*, vol. 12, no. 10, pp. 2175–2179, Oct. 2015. [Online]. Available: https://ieeexplore.ieee.org/lpdocs/epic03/wrapper.htm?arnumber=7169533
[65] X. Zhang, J. Zhou, F.-M. Gottsche, W. Zhan, S. Liu, and R. Cao, "A method based on temporal component decomposition for estimating 1-km all-weather land surface temperature by merging satellite thermal infrared and passive microwave observations," *IEEE Trans. Geosci. Remote Sens.*, vol. 57, no. 7, pp. 4670–4691, Jul. 2019, doi: 10.1109/TGRS.2019.2892417.
[66] A. Gemitzi, P. Dalampakis, and G. Falalakis, "Detecting geothermal anomalies using landsat 8 thermal infrared remotely sensed data," *Int. J. Appl. Earth Observ. Geoinf.*, vol. 96, Apr. 2021, Art. no. 102283, doi: 10.1016/j.jag.2020.102283.
[67] T. Lacava *et al.*, "Thermal monitoring of Eyjafjöll volcano eruptions by means of infrared MODIS data," *IEEE J. Sel. Topics Appl. Earth Observ. Remote Sens.*, vol. 7, no. 8, pp. 3393–3401, Aug. 2014, doi: 10.1109/JSTARS.2014.2330872.
[68] S. J. S. Khalsa, M. B. Dyurgerov, T. Khromova, B. H. Raup, and R. G. Barry, "Space-based mapping of glacier changes using ASTER and GIS tools," *IEEE Trans. Geosci. remote Sens.*, vol. 42, no. 10, pp. 2177–2183, Oct. 2004, doi: 10.1109/TGRS.2004.834636.
[69] D. K. Hall, "A review of the utility of remote sensing in Alaskan permafrost studies," *IEEE Trans. Geosci. Remote Sens.*, vol. GE-20, no. 3, pp. 390–394, Jul. 1982, doi: 10.1109/TGRS.1982.350460.
[70] J. Cheng, X. Meng, S. Dong, and S. Liang, "Generating the 30-m land surface temperature product over continental China and USA from landsat 5/7/8 data," *Sci. Remote Sens.*, vol. 4, Dec. 2021, Art. no. 100032, doi: 10.1016/j.srs.2021.100032.
[71] C. O. Justice *et al.*, "The Moderate Resolution Imaging Spectroradiometer (MODIS): Land remote sensing for global change research," *IEEE Trans. Geosci. Remote Sens.*, vol. 36, no. 4, pp. 1228–1249, Jul. 1998, doi: 10.1109/36.701075.
[72] R. Ghosh, P. K. Gupta, V. Tolpekin, and S. K. Srivastav, "An enhanced spatiotemporal fusion method—Implications for coal fire monitoring using satellite imagery," *Int. J. Appl. Earth Observ. Geoinf.*, vol. 88, Jun. 2020, Art. no. 102056, doi: 10.1016/j.jag.2020.102056.
[73] A. Hast, J. Nysjö, and A. Marchetti, "Optimal RANSAC—Towards a repeatable algorithm for finding the optimal set," *J. WSCG*, vol. 21, no. 1, pp. 21–30, 2013.

Xue Chen (Graduate Student Member, IEEE) received the M.Eng. degree in geomatics engineering from the China University of Geosciences, Beijing, China, in 2014. She is currently pursuing the Ph.D. degree in geomatics with the China University of Geosciences and in geosciences with the University of Padua, Padua, Italy.

Her research interests include technique developments of InSAR and their applications on geohazards.

Junhuan Peng received the B.S. degree in surveying and mapping and the M.S. degree in mine surveying from Central South University, Changsha, China, in 1985 and 1988, respectively, and the Ph.D. degree in geodesy and surveying engineering from Wuhan University, Wuhan, China, in 2003.

He is currently a Full Professor with the China University of Geosciences, Beijing, China. He is also the Director of the Shanxi Key Laboratory of Resources, Environment and Disaster Monitoring. His research interests include geological environment monitoring, disaster prevention and mitigation, and the application of spatial statistics and robust estimation in surveying engineering, imaging geodesy, and remote sensing.

Zeyang Song received the B.S. degree in safety engineering from the Hunan University of Science and Technology, Xiangtan, China, in 2008, and the M.S. and Ph.D. degrees in safety technology and engineering from the China University of Mining and Technology, Beijing, China, in 2011 and 2015, respectively.

He is currently an Associate Professor with the Xi'an University of Science and Technology, Xi'an, China. His research interests include hazard prevention and environmental protection in the energy and chemical industries.

Yueze Zheng received the B.S. degree in surveying engineering from Inner Mongolia Normal University, Hohhot, China, in 2016, and the M.S. degree in surveying and mapping from China University of Geosciences, Beijing, China, in 2019, where he is currently pursuing the Ph.D. degree in geomatics.

He is currently a Mid-Level Engineer with the Beijing Institute of Surveying and Mapping, Beijing, China. His research interests include InSAR data processing and subsidence monitoring.

Biyao Zhang received the Ph.D. degree from the China University of Geosciences, Beijing, China, in 2019.

He worked as a Post-Doctoral Fellow with the Aerospace Information Research Institute, Chinese Academy of Sciences, Beijing, from 2019 to 2021. He is currently an Associate Research Fellow with the Aerospace Information Research Institute, Chinese Academy of Sciences. His research interests include vegetation dynamic analysis and forest pest and disease monitoring.